



Effect of Electrochemical Potential on Tribocorrosion Behaviour of AISI 420

Andreas Gassner^{1,2} · Achim Conzelmann³ · Heinz Palkowski⁴ · Jürgen Wilde² · Hadi Mozaffari-Jovein^{1,3}

Received: 17 February 2022 / Revised: 31 May 2022 / Accepted: 13 June 2022 / Published online: 28 June 2022
© The Author(s), under exclusive licence to Springer Nature Switzerland AG 2022

Abstract

The effects of different electrochemical potentials on the tribocorrosive behaviour of AISI 420 in simulated body fluid (37 °C, 0.15 M NaCl solution) were studied, using a ball-on-disc tribometer under potentiostatic control. Results indicated a strong dependence of the material loss and degradation mechanisms on the applied potential. Cathodic polarization led to the lowest material loss, which was attributed to the electrochemical removal and mechanical destruction of the passive layer, resulting in a low corrosive degradation and strong adhesion. During polarization at the equilibria between cathodic and anodic reactions, maximum material loss was observed. This was attributed to galvanic coupling between the wear track and the surrounding surface, which resulted in a high electrochemical degradation, that was maintained by continuous mechanical destruction of the passive layer. At potentials in the passive region, a lower material loss was observed. This is considered to be caused by faster repassivation and higher stability of the passive layer, which inhibits electrochemical degradation and impedes the formation of adhesion contacts. According to the results, the greatest material destruction occurs in between cathodic or anodic polarisation, which is common during the use of products like surgical instruments.

Keywords Martensitic stainless steel · Tribocorrosion · Electrochemical potential · Wear loss · Sliding wear

1 Introduction

In many applications of medical technology, such as implants or instruments, tribological and electrochemical loads often co-exist, forming a tribocorrosive load collective, where mechanical wear and corrosive material removal can influence each other [1–6]. Due to their good mechanical properties and a high corrosion resistance in different media, stainless steels are often used under corrosive conditions.

However, frictional sliding in an electrolyte can weaken or destroy the passive layer or alter the near-surface microstructure, therefore increasing electrochemical material loss [1, 4–8]. Furthermore, products of the electrochemical reactions can have an abrasive or lubricating effect, resulting in an increase or decline of the tribological wear [9–12].

The complex tribocorrosive interactions were studied under a multitude of loads, identifying the electrochemical potential as one of the most influential parameters. Varying applied potentials modifies the electrochemical surface conditions by cathodically removing the existing passive layer, passively altering its composition and thickness or transpassively forming localized corrosion sites [12–16]. This influences the mechanical interaction and resulting wear between the frictional partners. Corresponding studies on austenitic stainless steels determined a potential-dependent material removal which was least pronounced under cathodic potentials, while anodic polarization showed an almost linear increase up to a factor of five, only dropping slightly when pitting corrosion occurred [14, 17]. These observations were mainly attributed to a potential-dependent transition in wear mechanisms, repassivation tendency and microstructure evolution [14, 17].

✉ Andreas Gassner
gassner-andreas@outlook.de

¹ STW Material-Technology, Take-Off Gewerbepark 9,
78579 Neuhausen ob Eck, Germany

² Department of Microsystems Engineering, University
of Freiburg, Georges-Köhler-Allee 103, 79110 Freiburg,
Germany

³ Institute of Materials Science and Engineering, Furtwangen
University Campus Tuttlingen, Kronenstraße 16,
78532 Tuttlingen, Germany

⁴ Institute of Metallurgy, Clausthal University of Technology,
Robert-Koch-Straße 42, 38678 Clausthal-Zellerfeld,
Germany

Martensitic stainless steels offer good mechanical properties and a moderate corrosion resistance and are therefore used in a variety of medical products facing tribocorrosive loads. However, only a few studies are currently available and demonstrate a deviating behaviour of the results. Zhang [15] and Huttunen-Saarivirta [18] found that although AISI 410 and 440B continued to exhibit the lowest material removal in the cathodic region, the maximum material loss shifted to the open circuit potential (OCP), dropping upon passive polarization. A lower repassivation tendency was held responsible, which led to increased corrosion and abrasive three-body wear. Passive polarization resulted in reduced corrosive material loss and a lubricating effect of the passive layer. In addition, Dalmau [8] discussed potential-dependent wear mechanisms and microstructure evolutions below the wear track as a possible factor for the observed behaviour. Cathodic polarization eliminates the passive layer allowing plastic flow with dislocation annihilation and limited wear [8]. In contrast, in the passive region, the build-up of dislocations at the interface to the passive layer led to severe grain refinement of the microstructure, facilitating formation of cracks and delamination [8].

Since the effect of the electrochemical potential on the tribocorrosive behaviour of martensitic stainless steels is insufficiently studied, the description of fundamental mechanisms of tribocorrosive material degradation is hindered.

However, martensitic stainless steels are commonly used in surgical instruments like scissors or needle holders, which allows interaction with different body fluids and load collectives, leading to the formation of different electrochemical potentials.

In this study, the influence of the electrochemical potential from the cathodic to the passive and transpassive regions on the tribocorrosive behaviour of AISI 420 martensitic stainless steel is investigated in NaCl solution to simulate body fluids.

2 Experimental Procedures

2.1 Material and Preparation

AISI 420 stainless steel, which is often applied in medical instruments like scissors, with a chemical composition as shown in Table 1, was used for the experiments. Square specimens with a side length of 50 mm and a thickness of 5 mm were cut from a steel sheet and subsequently ground from grit 180 to 2000. To generate a martensitic

microstructure, the specimens were austenitized under vacuum at 1025 °C, then quenched in gaseous nitrogen and tempered at 280 °C. The generated martensitic microstructure is shown in our previous study [19]. Heat treatment after grinding allowed prevention of possible subsurface deformations through preparation. Finally, polishing with 3 µm diamond suspension was performed.

2.2 Tribocorrosive Investigations

Tribocorrosive tests were carried out in a temperature-controlled electrochemical cell mounted to a universal tribometer that operated in the ball-on-disc modification. The test setup is shown in our previous study [19]. The tribometer consisted of different electrical drives and force sensors that allowed application and monitoring of the tribological load. Sapphire balls with a diameter of 5 mm were used as counter bodies.

The electrochemical cell was utilized in a three-electrode setup, containing the specimens as working electrode, a saturated Ag/AgCl electrode as reference and a platinum counter electrode that were connected via a potentiostat. The investigated sample surface was limited to 16.81 mm² by a Teflon gasket. To simulate conditions as in body fluids, 0.15 M NaCl solution tempered to 37 °C was used as electrolyte. All potentials given in this work refer to the utilized reference electrode.

Potentiodynamic polarization and Pourbaix diagrams were used to define relevant potentials for the tribocorrosive tests. At the beginning of each electrochemical characterization, the OCP was recorded for 1 h to allow stabilization. Afterwards, potentiodynamic polarization was performed from – 100 mV against OCP with a rate of 1 mV/s up to a limiting current density of 0.5 mA/cm². To determine the electrochemical behaviour under superimposed tribological load, a normal force of 15 N was applied between the counterbody and the specimen, simulating the contact pressure between two scissor blades. Subsequently a continuous circular motion with a radius of 4 mm at a frequency of 0.1 Hz was initiated based on studies determining the cutting speed of a surgeon [20]. Simultaneously, potentiodynamic polarization was performed using the described parameters. Based on the results, potentials at equilibrium, as well as in the cathodic, passive and transpassive range were selected for further investigations.

Tribocorrosive tests were carried out under potentiostatic control at the specified potentials. Initially the OCP of the samples was recorded over a period of 1 h to reach

Table 1 Chemical composition AISI 420 (mass %)

C	Cr	Mn	Si	P	S	Fe
0.22	12.90	0.43	0.156	0.01	<0.0005	Balance

equilibrium conditions. Electrochemical impedance spectroscopy (EIS) was performed at OCP with an amplitude of 10 mV in the frequency range from 100 mHz to 70 kHz, to evaluate the passive layer stability. Subsequently, the samples were potentiostatically polarized to the defined potentials, before sliding was initiated over 1000 cycles according to the previously described parameters. During the tribological loading, the current density over time and the coefficient of friction (COF) were recorded. On completion of the superimposed friction, OCP was measured for 1 h and EIS was performed using the described settings to examine the passive layer condition after the experiments. All experiments were repeated three times to ensure repeatability.

2.3 Material and Wear Characterization

The wear track morphology was assessed via light microscopy (LM) and scanning electron microscopy (SEM). In addition, the material loss was recorded by measuring the cross-sectional area of the wear track using a confocal laser scanning microscope. To evaluate the mechanical properties, Vickers microhardness measurements were performed in the wear track and on the nearby polished surface with a load of 0.5 N. In order to investigate the microstructure evolution below the damaged areas, longitudinal metallographic sections were observed by SEM after metallographic preparation and etching with Viella's reagent.

3 Results

3.1 Potentiodynamic Polarization Measurements

Figure 1 shows an example for the polarization behaviour of the samples in the absence and presence of a superimposed tribological load. In both cases, the curves can be

divided into a cathodic, an anodic-passive and an anodic-transpassive region, following the typical behaviour of passive stainless steels in NaCl-containing electrolytes. In the absence of friction, an OCP of -140 mV, a passive current density of 400 nA/cm² and a pitting potential of 156 mV were measured. When a tribological load was superimposed, the free corrosion potential shifted cathodically to a value of -280 mV, while the passive current density increased to 2.25 μ A/cm². The pitting corrosion potentials remained constant. The shift of the values indicates a mechanically induced destruction of the passive layer, which results in a local activation of the material and consequently formation of a galvanic element, leading to a decrease of the potential and higher current densities [1, 11–13].

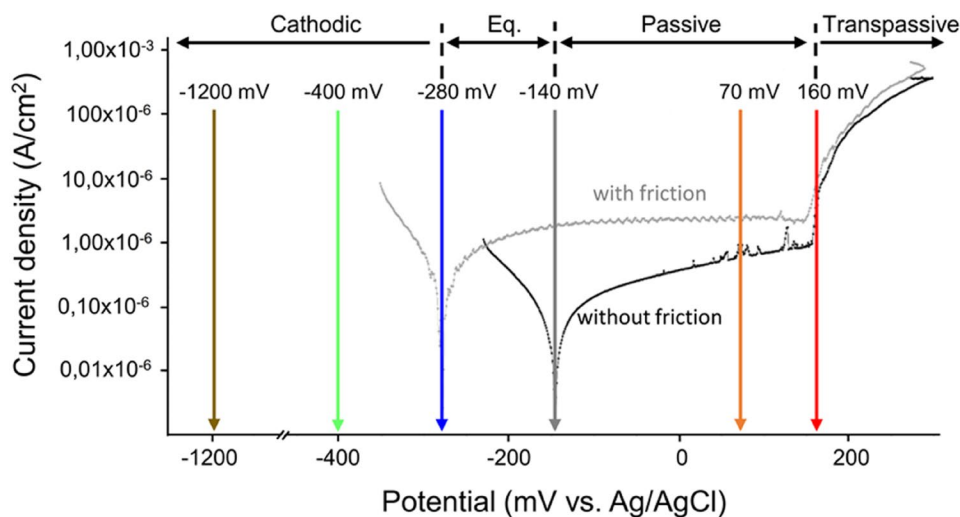
Considering the determined polarization curves and Pourbaix diagrams of iron and chromium (Fig. 2) in aqueous media, six potentials over the different reaction ranges were selected for further tribocorrosive investigation. The cathodic range was covered by potentials of -1200 mV and -400 mV. The cathodic/anodic transition was addressed by the equilibrium potentials with and without tribological load at -280 mV and -140 mV (OCP). In the passive and transpassive range, 70 mV as well as 160 mV were chosen. All defined potentials are colour-coded in the corresponding figures.

3.2 Tribocorrosive Behaviour

3.2.1 Current Density Over Time

Figure 3 illustrates the current density over time recorded during the potentiostatic tests. Potentials lower than -280 mV exhibited a permanently negative, cathodic current density, where no anodic metal dissolution and therefore corrosion was active. Polarization at -280 mV led to a negative current density, that slowly rose towards a value

Fig. 1 Potentiodynamic polarisation curves of AISI 420 under corrosive (black) and tribocorrosive loads (grey) with indicated test potentials



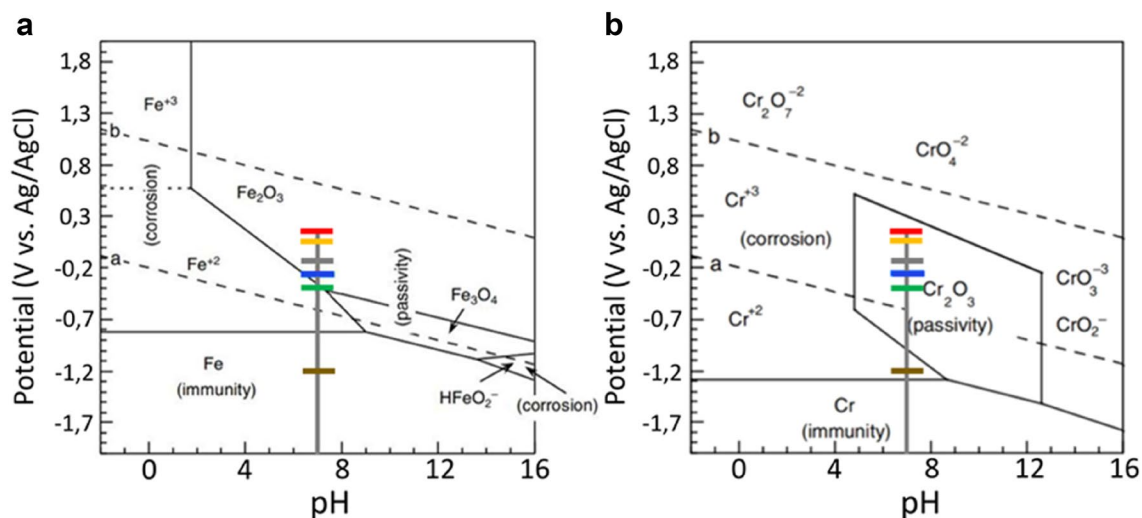
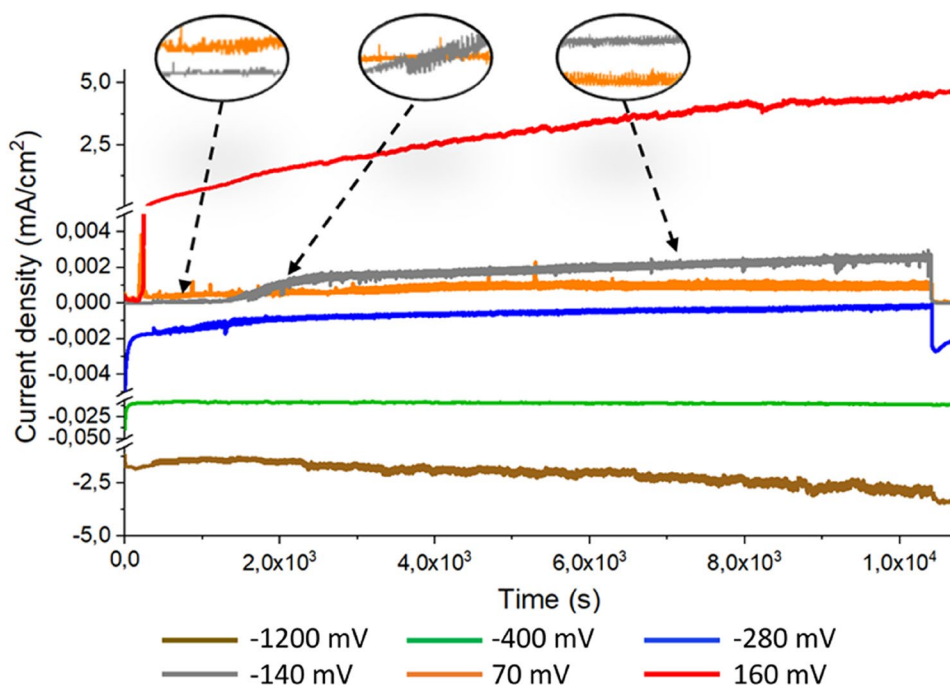


Fig. 2 Pourbaix diagrams of iron (a) and chromium (b) in aqueous solution [21] with indicated test potentials

Fig. 3 Current density over time during tribocorrosive load at applied potentials



of zero, dropping sharply after removal of the tribological load. The applied polarizations at -140 mV (OCP), as well as in the passive range (70 mV), resulted in a positive current density, which increased significantly at the onset of the tribological load and fell after termination. The positive currents indicated anodic metal dissolution. In addition, a new behaviour could be observed, which is shown in the magnified areas of the illustration. While initial current densities at 70 mV were higher than the value at -140 mV, after an experimental time of about 1800 s, the order reversed, indicating stronger electrochemical dissolution in equilibrium. Observing the sample held at 160 mV in the transpassive

region, a sudden increase in the current density could be noted with the onset of polarization, which became larger as the experiment continued. In addition, the value of the current density did not decrease after the completion of the experiment but instead continued to increase steadily. This indicates electrochemical metal dissolution even after polarization has been discontinued.

The present sinusoidal variation, which was also visible in the potentiodynamic curves, can be attributed to the circular movement of the counterbody and the associated electrochemical change of the wear track, while the reference electrode remained static.

3.2.2 Electrochemical Impedance Spectroscopy

Quantitative impedance data (Table 2) were determined by fitting the EIS data to a Randles equivalent circuit that was modified by a constant phase element (CPE) visualized in Fig. 4. R_s shows the solution resistance of the electrolyte, R_p the polarization resistance of the passive layer and the CPE is used to describe the double layer capacity, while n evaluates how close CPE is to an ideal capacity ($n = 1$) [22, 23]. Compared to the reference measurement prior to tribocorrosive exposure, the sample polarized at -400 mV showed similar shapes, leading to a similar value of R_p . At -280 mV, 160 mV and -1200 mV, a continuous decline in the R_p was noticed, which revealed a decreased passive layer stability. In contrast, the experiments at -140 mV and 70 mV resulted in an increased R_p , revealing higher stability

of the passive films. CPE values negatively correlated to the R_p , therefore indicating high ion concentration and rising capacity of the electrochemical double layer when passive layer stability diminishes.

3.2.3 Optical Appearance

Figure 5 displays LM and SEM images of the wear track morphologies. In case of strong cathodic polarization at -1200 mV, a small wear track with a width of $160 \mu\text{m}$ was observed showing abrasion and pitting corrosion. The pitting occurred only after the termination of polarization and was attributed to acidification of the electrolyte as a result of polarization-induced hydrogen evolution [17, 24]. At cathodic polarization of -400 mV, the width of the wear track rose to $190 \mu\text{m}$, while material transfers, shear cracks

Table 2 Impedance parameters determined from fitted EIS spectra

Potential (mV _{Ag/AgCl})	R_s ($\Omega \text{ cm}^2$)	R_p ($\Omega \text{ cm}^2$)	CPE ($\Omega^{-1} \text{ cm}^{-2} \text{ s}^n$)	n
Reference	21 ± 15.0	$(227 \pm 1.6) \times 10^3$	$(38 \pm 5.0) \times 10^{-6}$	0.93 ± 0.01
-1200	9.2 ± 2.8	$(1.22 \pm 0.08) \times 10^3$	$(127 \pm 4.1) \times 10^{-6}$	0.77 ± 0.02
-400	10.5 ± 1.0	$(263 \pm 22.0) \times 10^3$	$(39 \pm 0.9) \times 10^{-6}$	0.93 ± 0.01
-280	13.6 ± 9.5	$(167 \pm 81.0) \times 10^3$	$(49 \pm 6.2) \times 10^{-6}$	0.88 ± 0.01
-140	5.0 ± 1.6	$(339.5 \pm 3.5) \times 10^3$	$(36 \pm 0.1) \times 10^{-6}$	0.91 ± 0.01
70	21.8 ± 0.7	$(424.0 \pm 34) \times 10^3$	$(32 \pm 2.0) \times 10^{-6}$	0.93 ± 0.01
160	20.4 ± 13.5	$(10.0 \pm 1.6) \times 10^3$	$(172 \pm 24) \times 10^{-6}$	0.93 ± 0.01

Fig. 4 Nyquist plots of EIS after the tribocorrosive load at applied potentials

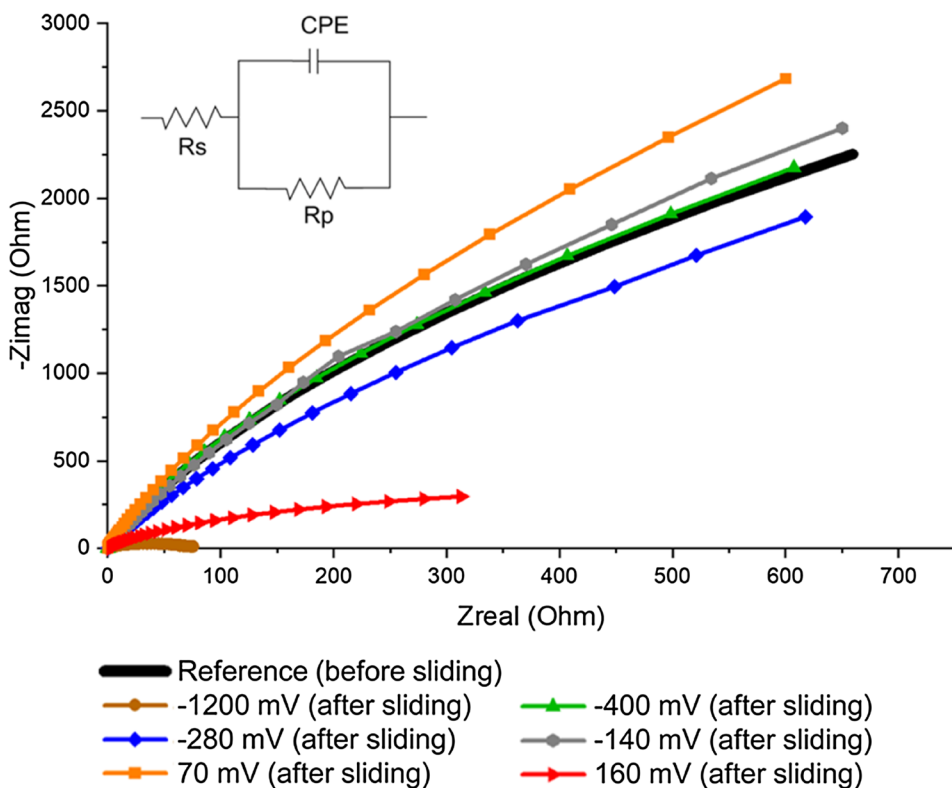
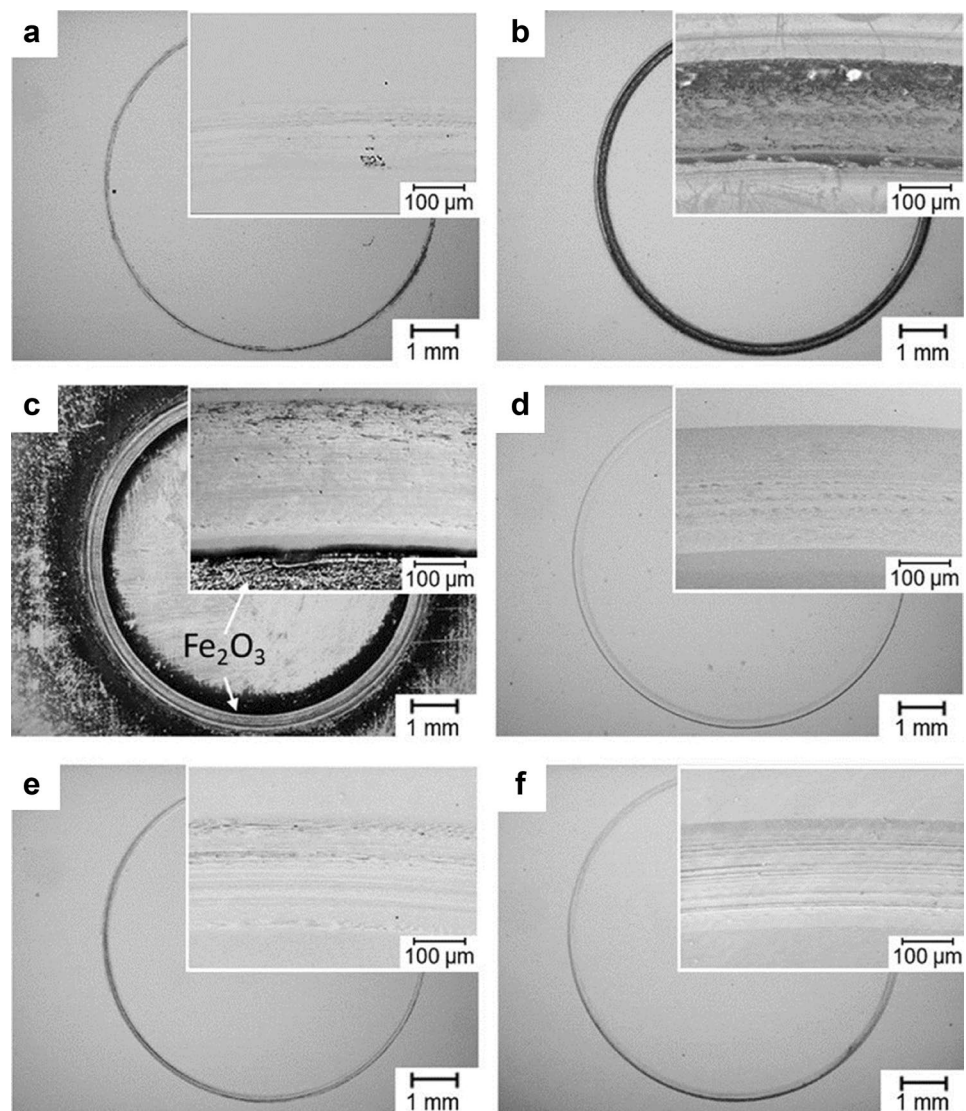


Fig. 5 LM micrographs and magnified SEM sections of the wear tracks, **a** – 1200 mV, **b** – 400 mV, **c** – 280 mV, **d** – 140 mV, **e** 70 mV, **f** 160 mV



and Fe_2O_3 deposits were identified. The sample at equilibrium conditions in the presence of friction (– 280 mV) showed a different behaviour. The wear track widened significantly to 287 μm and showed fine grooves that merged into small amounts of transferred material at the edges. In addition, a heavy deposit of Fe_2O_3 was identified next to the wear track. With polarization into the passive, as well as transpassive region, wear track width decreased to 200 μm and 202 μm , while deep grooves were visible.

3.2.4 Microstructural Evolution

Tribocorrosive loading led to material deformation with a microstructure evolution underneath the wear track, as shown in the SEM micrographs in Fig. 6. The heat-treated AISI 420 is composed of hierarchically arranged martensite laths and precipitated chromium-rich carbides, which is explained in further detail in [19]. As indicated by the red

lines in Fig. 6, plastic deformation revealed an inclination of the martensite laths in loading direction, which varied with the applied potentials. At – 1200 mV, an affected zone of 7 μm was visible, while at – 400 mV, a maximal deformation of 10 μm could be measured. Polarized to – 280 mV, the depth of the influenced microstructure decreased to just 1 μm . With increasing polarization from – 140 to 70 and 160 mV, the value rose slightly from 3 to 5 μm .

3.2.5 Hardness

The deformation under tribocorrosive loading with varying polarization led to increased hardness values, as shown in Fig. 7. For strongly cathodically polarized samples, almost no difference to the reference of 545 HV was observed. At higher polarization, the hardness increased almost linearly to a value of 787 HV at 160 mV. An exception was observed at – 280 mV delivering a value deviating from the linearity.

Fig. 6 SEM images of the deformed microstructures above the dashed lines in longitudinal sections through the wear tracks **a** – 1200 mV, **b** – 400 mV, **c** – 280 mV, **d** – 140 mV, **e** 70 mV, **f** 160 mV (Color figure online)

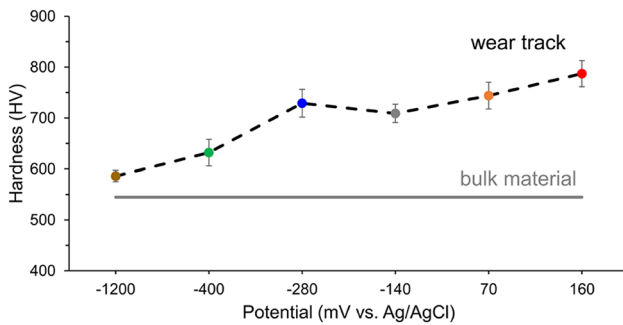
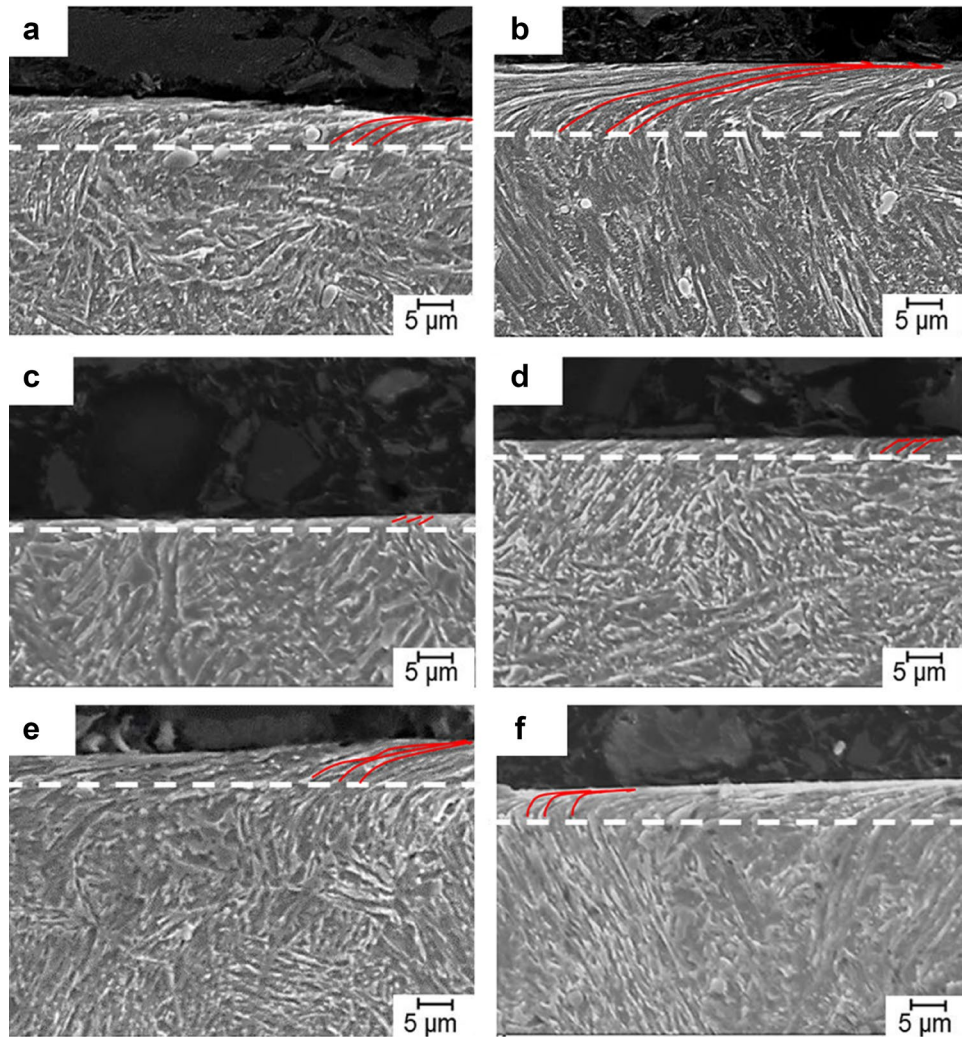


Fig. 7 Hardness values in the wear track after tribocorrosive tests at applied potentials

3.3 Material Loss and COF

Material loss and friction coefficients at the applied potentials are illustrated in Fig. 8. The trend of the values is in line with the results of previous studies by Zhang [12, 15]. Under cathodic polarization at – 1200 mV, the material loss

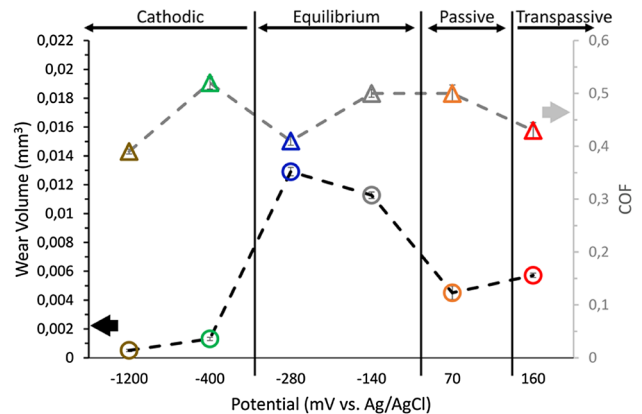


Fig. 8 Total material loss and COF as a function of applied potentials

(0.0005 mm³) and the COF showed minimum values. By raising the potential to – 400 mV, the determined material loss increased to 0.0013 mm³ and the friction coefficient reached its maximum value. At – 280 mV, a tenfold increase

in the measured material loss to the highest recorded amount of 0.013 mm^3 was coupled with a lower COF. With rising potentials, the material loss decreased to 0.011 mm^3 at -140 mV and a local minimum of 0.0045 mm^3 at 70 mV , while the COF increased slightly. In the transpassive region, a wear volume of 0.0057 mm^3 and a decreasing COF were measured.

4 Discussion

The results indicated a clear dependence of the material loss and effective degradation mechanisms on the applied potentials.

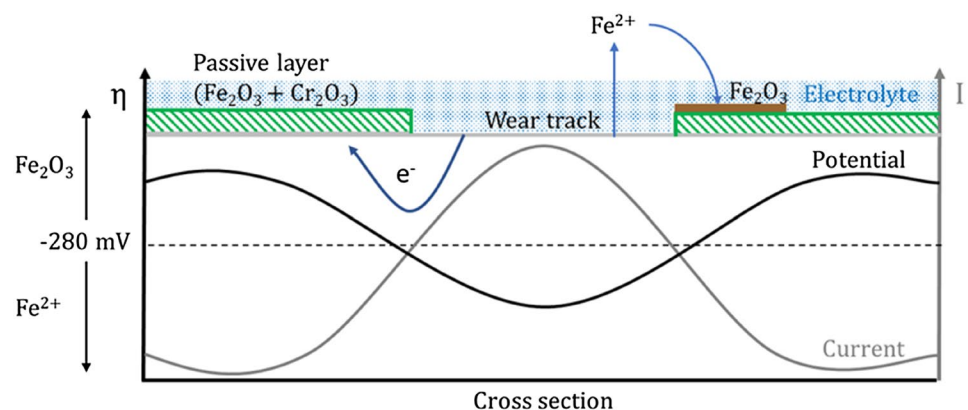
Under cathodic polarization into the immune area (Fig. 2) and thus absent anodic metal dissolution, the lowest material loss (Fig. 8) at -1200 mV was observed. Furthermore, the appearance and wear mechanisms within the wear tracks of the cathodic polarized samples varied. While abrasion could mainly be detected at -1200 mV , weaker cathodically polarized (-400 mV) specimens showed strong adhesion phenomena. This behaviour can be attributed to the potential dependence of the surface condition and electrochemical reactions [12–16]. Polarization at -1200 mV was accompanied by a large evolution of hydrogen in the wear track which could adsorb and penetrate the material surface. In this process, adsorption or gas formation can act as a barrier to reduce the interaction between specimen and counter body [25, 26], while diffusion into the material can lead to local embrittlement accompanied by a decrease in ductility and adhesion tendency [15, 24–28]. This leads to a low COF as well as small subsurface material alteration. In sum, the lack of electrochemical dissolution combined with the low interaction strength results in the lowest material loss.

At a polarisation of -400 mV , no hydrogen evolution was evident. Due to continuing cathodic degradation and mechanical destruction of the passive layer, a direct contact between the counterbody and the test specimen was possible. This enables the formation of adhesive junctions, as

indicated by the high COF, that transfer high shear stresses into the subsurface, initiating strong deformation and adhesive wear. In the absence of the passive layer, dislocations can be annihilated at the surface, promoting strong microstructural deformation without forming cracks [1, 18]. The low material loss can thus be attributed to missing electrochemical material removal and slight work hardening of the microstructural areas near the surface.

Polarisation to -280 mV drastically changed the observed effects. Compared to cathodic polarization, the material loss increased by a factor of ten, while the friction coefficient dropped significantly, showing mainly abrasive wear. Furthermore, a strong deposition of Fe_2O_3 was found next to the wear track. This is probably triggered by the applied potential, as the Pourbaix diagrams indicate that the potential lies near the boundary region between stable Fe_2O_3 formation and Fe^{2+} evolution (Fig. 2). The superimposed tribological load can locally destroy the passive layer and electrochemically activate the material. This results in a potential drop within the wear track into the existence range of Fe^{2+} ions, enabling iron dissolution. Microgalvanic coupling with the surrounding surface slightly increases the potential outside the track, allowing Fe_2O_3 to be formed. The effect therefore causes iron to dissolve as Fe^{2+} ions within the wear track and to be oxidized directly to Fe_2O_3 at the edges of the wear track while oxygen is reduced. The resulting galvanic element is associated with a high current across the interface and ultimately results in a rapid electrochemical material removal. The processes described are shown graphically in Fig. 9. This correlates with the measured current density curve in Fig. 3, which increased with time and thus indicates an interaction between the activated track and the surface surrounding it. The continuous removal of material can also expose carbides, which in combination with the Fe_2O_3 formed next to the track can lead to three-body wear resulting in increased mechanical abrasion. Carbides and oxide particles being present in the contact area combined with a Cr_2O_3 passive layer prevent adhesive bondings, resulting in the low COF. The combination of rapid electrochemical

Fig. 9 Schematic potential and current curves across the wear track at -280 mV during tribo-corrosive testing



dissolution and low interaction between the counterbody and the specimen also results in a very small microstructural change below the surface.

In the passive range from -140 mV (OCP) to 70 mV, another significant transition in damage mechanisms could be identified. With increasing potential, a slight decrease in material loss, a constant COF, deeper grooves and a higher hardness were observed. This behaviour can be explained by considering the electrochemical surface conditions and the deformed microstructure. At higher anodic potentials, passive layer formation is favoured, increasing the repassivation rate and probably changing its composition [13, 29]. By EIS measurements, an increased R_p could be determined after the experiment at 70 mV, attributed to an increased passive film stability [22, 23], which increases the resistance towards the applied tribological load and accelerates the repassivation in the case of mechanical damage. As a result, the measured current density remains almost constant at 70 mV, while at the OCP, due to the lower stability of the passive layer and its slower repassivation, a continuous increase in the current and thus in the electrochemical activity was observed. In addition, according to current research, the passive layer can influence the deformation mechanism in the near-surface zone [30–32]. The contacting relative motion induces shear stresses, which lead to the formation of dislocations, that can accumulate at the passive layer interface and arrange in so-called dislocation cells. These cells can be described as subgrains of a few nanometers in size, acting as severe obstacles for newly formed dislocations and result in a significant increase in hardness [19, 30–32]. In combination with a reduced interaction between the sphere and the specimen due to the stronger passive layer, the hardened specimen surface results in a low material removal with an abrasive appearance [33–35]. In addition, oxides occurring in the passive layer can possibly have a lubricating effect [36]. It can therefore be stated that an increased anodic polarization in the passive region leads to a more stable, rapidly forming passive layer with an underlying refined microstructure, which in combination can counteract both electrochemical and mechanical material removal.

At 160 mV, an increased material loss was observed, which can be attributed primarily to the increased electrochemical material removal that was visible in the abrupt increase of the current density curve (Fig. 3). When polarized beyond the passive region, the passive layer is locally destroyed and the resistance to metal dissolution is reduced. This results in the formation of pitting corrosion sites where a large amount of material can be transferred to the electrolyte in a short time. In addition, the repassivation of the wear track is hindered by the tribological load, as can be seen through the results of EIS, in which a greatly reduced R_p is visible. In addition, corrosive attacks can dissolve chromium-depleted areas around chromium-rich carbides

within the wear track [37, 38], whereby the hard carbides get between specimen and counter body developing an abrasive effect. Due to the mentioned effects, strong abrasive grooves are formed and the material loss increases.

This study confirmed the observed trends in the material loss and COF found by Zhang et al. [12, 15] for AISI 410 stainless steel in artificial sea water and expanded the investigation of the mechanisms using wider potential ranges. Comparing different studies in tribocorrosion is very complicated, since the examined materials and load collectives differ widely. This limits the study, since a wider range of load collectives as well as additional measurements like XPS or TEM of the deformed surface microstructure are needed to fully understand the underlying mechanisms.

5 Conclusions

In this study, the influence of the electrochemical potential on the tribocorrosive behaviour of AISI 420 in simulated body fluid was investigated. The results demonstrate a strong dependence of the material loss and the acting mechanisms on the applied electrochemical potential.

- (1) Cathodic polarization at -1200 mV led to the lowest material loss and COF, while abrasive wear was detected. This is presumably caused by the absence of electrochemical material removal and a hydrogen-induced low interaction strength between specimen and counterbody.
- (2) While the material loss at -400 mV remained low due to the absence of electrochemical material removal, the highest COF and strong adhesive wear with a resulting deep deformation of the subsurface microstructure were observed. This can be attributed to electrochemical degradation of the passive layer in combination with a lack of hydrogen evolution leading to strong adhesive bondings.
- (3) By polarization to -280 mV, the material loss increased abruptly to the maximum value, while the COF dropped significantly. Abrasive grooves in and Fe_2O_3 deposits next to the wear track were detected, as the deformation of near-surface microstructural regions remained absent. This is presumably caused by a local galvanic coupling between wear track and surrounding surface leading to high electrochemical material loss.
- (4) Following polarization at the passive region, the material loss decreased and the COF remained stable. Fine abrasive grooves and a strongly deformed microstructure were observed. This can be attributed to the formation of a more stable passive layer, which can be stated by the EIS measurements and is associated with faster repassivation and accumulation of dislocations.

- (5) Transpassive polarization led to an increase in material loss and deep abrasive grooves, which is caused by local breakdown of the passive layer and exposing of abrasive chromium-rich carbides in the wear track.

Funding There were no research grants from any funding agencies for this work.

Data Availability All data generated or analysed during this study are included in this published article.

Declarations

Conflict of interest The authors have no relevant financial or non-financial interests to disclose.

References

- Landolt D, Mischler S (2011) Tribocorrosion of passive metals and coatings. Woodhead Publishing Limited, Cambridge
- Yan Y (2013) Bio-tribocorrosion in biomaterials and medical implants. Woodhead Publishing Limited, Cambridge
- Menezes PL, Ingole SP et al (2013) Tribology for scientists and engineers. Springer, New York
- Wood R (2007) Tribo-corrosion of coatings: a review. *J Phys D Appl Phys*. <https://doi.org/10.1088/0022-3727/40/18/S10>
- Dalmau A, Richard C, Igual-Munoz A (2018) Degradation mechanisms in martensitic stainless steels: wear, corrosion and tribocorrosion appraisal. *Tribol Int* 121:167–179. <https://doi.org/10.1016/j.triboint.2018.01.036>
- Mischler S, Spiegel A, Landolt D (1999) The role of passive oxide films on the degradation of steel in tribocorrosion systems. *Wear* 225–229:1078–1087. [https://doi.org/10.1016/S0043-1648\(99\)00056-3](https://doi.org/10.1016/S0043-1648(99)00056-3)
- Yin C, Liang Y, Jiang Y, Yang M, Long S (2017) Formation of nano-laminated structures in a dry sliding wear-induced layer under different wear mechanisms of 20CrNi2Mo steel. *Appl Surf Sci* 423:305–313. <https://doi.org/10.1016/j.apsusc.2017.06.187>
- Dalmau A, Rmili W, Richard C, Igual-Munoz A (2016) Tribocorrosion behavior of new martensitic stainless steels in sodium chloride solution. *Wear* 368–369:146–155. <https://doi.org/10.1016/j.wear.2016.09.002>
- Boese E, Röthig J, Garz I, Schmidtchen H (1998) Tribokorrosion von nichtrostenden Stählen. *Mater Corros* 49:98–107. [https://doi.org/10.1002/\(SICI\)1521-4176\(199802\)49:2%3C98::AID-MACO98%3E3.0.CO;2-7](https://doi.org/10.1002/(SICI)1521-4176(199802)49:2%3C98::AID-MACO98%3E3.0.CO;2-7)
- Watson SW, Friedersdorf FJ, Madsen BW, Cramer SD (1995) Methods of measuring wear-corrosion synergism. *Wear* 181–183:476–484. [https://doi.org/10.1016/0043-1648\(95\)90161-2](https://doi.org/10.1016/0043-1648(95)90161-2)
- Mischler S (2008) Triboelectrochemical techniques and interpretation methods in tribocorrosion: A comparative evaluation. *Tribol Int* 41:573–583. <https://doi.org/10.1016/j.triboint.2007.11.003>
- Zhang BB, Wang JZ, Zhang Y, Han GF, Yan FY (2017) Tribocorrosion behavior of 410SS in artificial seawater: effect of applied potential. *Mater Corros* 68:295–305. <https://doi.org/10.1002/maco.201609119>
- Olsson COA, Landolt D (2003) Passive films on stainless steels - chemistry, structure and growth. *Electrochim Acta* 48:1093–1104. [https://doi.org/10.1016/S0013-4686\(02\)00841-1](https://doi.org/10.1016/S0013-4686(02)00841-1)
- Sun Y, Rana V (2011) Tribocorrosion behaviour of AISI 304 stainless steel in 0.5 M NaCl solution. *Mater Chem Phys* 129:138–147. <https://doi.org/10.1016/j.matchemphys.2011.03.063>
- Zhang B, Wang J, Zhang Y, Han G, Yan F (2016) Comparison of tribocorrosion behaviour between 304 austenitic and 410 martensitic stainless steels in artificial seawater. *RSC Adv* 6:107933–107941. <https://doi.org/10.1039/C6RA18497A>
- Bidiville A, Favero M, Stadelmann P, Mischler S (2007) Effect of surface chemistry on the mechanical response of metals in sliding tribocorrosion systems. *Wear* 263:207–217. <https://doi.org/10.1016/j.wear.2007.01.066>
- Sun Y, Haruman E (2011) Effect of electrochemical potential on tribocorrosion behavior of low temperature plasma carburized 316L stainless steel in 1 M H₂SO₄ solution. *Surf Coat Technol* 205:4280–4290. <https://doi.org/10.1016/j.surfcoat.2011.03.048>
- Huttunen-Saarivirta E et al (2016) Tribocorrosion study of martensitic and austenitic stainless steels in 0.1 M NaCl solution. *Tribol Int* 95:358–371. <https://doi.org/10.1016/j.triboint.2015.11.046>
- Gassner A et al (2021) Tribocorrosion mechanisms of martensitic stainless steels. *HTM J Heat Treat Mater* 76:205–218. <https://doi.org/10.1515/htm-2021-0004>
- Greenish S et al (2002) Measurement, analysis and display of haptic signals during surgical cutting. *Presence* 11:626–651. <https://doi.org/10.1162/105474602321050749>
- McCafferty E (2010) Introduction to corrosion science. Springer, New York
- Diomidis N, Celis JP, Ponthiaux P, Wenger F (2009) A methodology for the assessment of the tribocorrosion of passivating metallic materials. *Lubr Sci* 21:53–67. <https://doi.org/10.1002/ls.73>
- Dalbert V et al (2019) The effects of microstructures and repassivation kinetics on the tribocorrosion resistance of ferrite and ferrite-martensite stainless steels. *Wear* 420–421:245–256. <https://doi.org/10.1016/j.wear.2018.10.023>
- Favero M, Stadelmann P, Mischler S (2006) Effect of the applied potential of the near surface microstructure of a 316L steel submitted to tribocorrosion in sulfuric acid. *J Phys D Appl Phys* 39:3175–3183. <https://doi.org/10.1088/0022-3727/39/15/S07>
- Grzeskiewicz R (1988) Effect of hydrogen on the coefficient of friction of iron. Virginia Polytechnic Institute and State University, Blacksburg
- Pokhmurs'kyi VI, Vasylyv KB (2012) Influence of hydrogen on the friction and wear of metals (a survey). *Mater Sci* 48:125–138. <https://doi.org/10.1007/s11003-012-9482-1>
- Siddiqui RA, Abdullah HA (2005) Hydrogen embrittlement in 0.31 % carbon steel used for petrochemical applications. *J Mater Process Technol* 170:430–435. <https://doi.org/10.1016/j.jmatp.2005.05.024>
- Kheradmand N et al (2016) Effect of hydrogen on the hardness of different phases in super duplex stainless steel. *Int J Hydrogen Energy* 41:704–712. <https://doi.org/10.1016/j.ijhydene.2015.10.106>
- Haupt S, Strehblow HH (1995) A combined surface analytical and electrochemical study of the formation of passive layers on Fe/Cr alloys in H₂SO₄. *Corros Sci* 37:43–54. [https://doi.org/10.1016/0010-938X\(94\)00104-E](https://doi.org/10.1016/0010-938X(94)00104-E)
- Liu Z (2018) Microstructure evolution under tribological loading and its elementary mechanisms. Karlsruhe Institut für Technologie Fakultät Maschinenbau. <https://doi.org/10.5445/IR/1000085322>
- Battaile CC et al (2012) The hardness and strength of metal tribofilms: an apparent contradiction between nanoindentation and

- pillar compression. *Acta Mater* 60:1712–1720. <https://doi.org/10.1016/j.actamat.2011.11.059>
32. Wang Y, Lei T, Liu J (1999) Tribo-metallographic behavior of high carbon steels in dry sliding—III. Dynamic microstructural changes and wear. *Wear* 231:20–37. [https://doi.org/10.1016/S0043-1648\(99\)00117-9](https://doi.org/10.1016/S0043-1648(99)00117-9)
 33. Sikorski ME (1963) Correlation of the coefficient of adhesion with various physical and mechanical properties of metals. *J Basic Eng.* <https://doi.org/10.1115/1.3656577>
 34. Sikorski ME (1964) The adhesion of metals and factors that influence it. *Wear* 7:144–162. [https://doi.org/10.1016/0043-1648\(64\)90050-X](https://doi.org/10.1016/0043-1648(64)90050-X)
 35. Mokhtar MOA, Zaki M, Shawki GSA (1980) Correlation between the frictional behaviour and the physical properties of metals. *Wear* 65:29–34. [https://doi.org/10.1016/0043-1648\(80\)90004-6](https://doi.org/10.1016/0043-1648(80)90004-6)
 36. Stott FH, Wood GC (1978) The influence of oxides on the friction and wear of alloys, Veröffentlichung. *Tribol Int.* [https://doi.org/10.1016/0301-679X\(78\)90178-0](https://doi.org/10.1016/0301-679X(78)90178-0)
 37. Anantha KH et al (2017) In situ AFM study of localized corrosion processes of tempered AISI 420 martensitic stainless steel: effect of secondary hardening. *J Electrochem Soc* 164:810–818. <https://doi.org/10.1149/2.1261713jes>
 38. Anantha KH (2018) An experimental study to understand the localized corrosion and environment assisted cracking behavior of AISI 420 martensitic stainless steel. KTH Royal Institute of Technology, Stockholm

Publisher's Note Springer Nature remains neutral with regard to jurisdictional claims in published maps and institutional affiliations.